

VALIDATION OF QUANTITATIVE BOUND AND PORE WATER IMAGING IN
CORTICAL BONE

By

Mary Katherine Manhard

Thesis

Submitted to the Faculty of the
Graduate School of Vanderbilt University
in partial fulfillment of the requirements
for the degree of

MASTER OF SCIENCE

in

Biomedical Engineering

May, 2013

Nashville, Tennessee

Approved:

Mark D. Does

Adam Anderson

ACKNOWLEDGEMENTS

I would like to thank my funding source, NIH grant number EB014308, and my advisor Dr. Mark Does, for his extensive guidance and support as a teacher and a mentor. I would also like to thank my lab mates for their support with this project.

LIST OF FIGURES

Figure

1.	Variable Flip Angle Approach.....	11
2.	Accounting for Signal Loss Due to Relaxation Induced Blurring.....	14
3.	Pulse Sequence Diagram.....	16
4.	Representative 3D Imaging Results.....	20
5.	Representative NMR Spectrum	21
6.	Comparison of Imaging Results to CPMG Measures.....	22

TABLE OF CONTENTS

	Page
ACKNOWLEDGEMENTS	ii
LIST OF FIGURES	iii
Chapter	
I. INTRODUCTION	1
I.1 Background and Motivation	1
I.2 Nuclear Magnetic Resonance (NMR) Studies of Cortical Bone.....	3
I.2.1 Characterization of NMR Signal in Cortical Bone.....	3
I.2.2 NMR of Cortical Bone and Mechanical Properties.....	5
I.2.3 Adiabatic Pulse Methods	6
I.3 MRI for Cortical Bone Imaging	8
I.3.1 Ultra-short Echo Time (UTE) Imaging	8
I.3.2 Variable Flip Angle Approach	9
I.3.3 Signal Amplitude Correction for Blurring.....	11
I.3.4 Bound and Pore Water Imaging	14
II. MATERIALS AND METHODS.....	15
II.1 Pulse Sequences	15
II.2 Data Analysis	17
III. RESULTS	20
IV. DISCUSSION AND CONCLUSIONS	23
REFERENCES	27

CHAPTER I

INTRODUCTION

I.1 Background and Motivation

Bone fractures are a widespread problem that affects over 10 million people each year in the United States (1). Increases in bone fractures are often related to problems such as diabetes and aging (2–6). The costs associated with bone fracture risks are over \$17 billion per year in the United States, and with the aging of the U.S. population, costs are expected to increase by 50% by the year 2025 (1). Likewise, the prevalence of diabetes is increasing rapidly (7), leading to even higher costs and an increasing need for comprehensive clinical procedures to accurately measure and diagnose fracture risk.

The current clinical methods for evaluating bone health do not fully predict fracture risk in bone, as they only investigate the mineral composition of bone. As a result, there is a need for improved diagnostic methods for measuring bone fracture risk. The work presented here validates methods for using Magnetic Resonance Imaging (MRI) to measure cortical bone water and shows promising results for advancement in clinical fracture risk assessment.

Human bone is comprised of osseous tissue that is hard, lightweight and made mostly of calcium phosphate and a collagen network. The calcium phosphate component of bone gives it its strength, but is also extremely brittle. Collagen fibers give bone elasticity, and both the strength and elasticity of bone help to increase fracture resistance. Bone fracture risk increases for a variety of reasons, including bone diseases, diabetes, aging, and during bone fracture healing.

Fracture risk increase is usually attributed to a decrease in bone mineral density (BMD), which can be measured by Dual X-ray Absorptiometry (DXA) and quantitative Computed Tomography (qCT). DXA obtains x-rays at two different energy levels and subtracts soft tissue components to get a BMD measure on an areal basis. qCT uses phantoms with known BMD levels measured concurrently with conventional CT of bones so that the bone signal can be converted into BMD over the entire volume. DXA is less expensive and easier to do, but does not provide the volumetric measures that qCT gives. Volumetric measures help determine whole bone mechanical properties, such as cross sectional moment of inertia and cortical bone thickness (8–10). These properties can be used in finite element modeling to help better determine fracture risk (11–13). However, both DXA and qCT methods only measure the mineral composition of bone, and do not account for soft tissue components such as collagen and pore water.

Changes in collagen content or condition also affect fracture risk. For example, as a person ages, the collagen content of their bones decreases which results in increased brittleness of the bone (14,15), leading to a significant increase in fracture risk. The collagen content of bones can not be measured with standard X-ray based methods, but MRI has the ability to measure both the water bound to collagen (bound water) and the water existing in the pores of the bones (pore water), giving it an advantage as a fracture risk predictor.

Developing MRI based methods to evaluate bone fracture risk yields better and safer imaging methods for treatment planning in cases of osteoporosis, diabetes, and other diseases associated with increased bone fracture. MRI methods that can measure soft-tissue characteristics of bone offer a fundamentally new diagnostic measure of bone

which may be valuable in researching the mechanisms of increased fracture risk or in development of drugs to treat such risks.

I.2 NMR Studies of Cortical Bone

I.2.1 Characterization of NMR Signal in Cortical Bone

Before imaging methods were developed, non-imaging methods with ^1H Nuclear Magnetic Resonance (NMR) were used to characterize the proton signal from cortical bone. NMR has been used to determine microstructural characteristics of many types of porous materials (16–18), and has also been applied to human cortical bone in many studies (19–22). NMR proton spin-spin (T_2) relaxation time measurements can be used to assess cortical bone. Longer T_2 relaxation times generally correspond to a larger pore size, so a range of T_2 values are expected for pore water. Water bound to collagen is expected to have a short T_2 relaxation time (23), and protons from collagen itself are expected to have even shorter T_2 relaxation times. When using NMR, a T_2 spectrum is produced, showing the relative number of protons across the T_2 values.

It was determined that ^1H NMR distinguished signals from pore water, bound water, collagen, and lipids in cortical bone based on their T_2 times (23). These results came from a study of small cadaveric cortical bone samples studied using Carr-Pucell-Meiboom-Gill (CPMG) (24) ^1H NMR measurements to measure the T_2 spectrum. The spectrum showed three distinct components that were further characterized by additional NMR studies.

The samples underwent an inversion recovery prepared CPMG (IR-CPMG) measurements to determine T_1 - T_2 spectra, T_2 - T_2 relaxation exchange spectroscopy

(REXSY) (25) to observe the magnetization transfer between proton pools, and deuterium oxide (D_2O) immersion to wash out freely exchanging 1H signal components. Two dimensional T_1 - T_2 spectra show T_1 versus T_2 relaxation times for all components of the samples. Two dimensional T_2 - T_2 REXSY plots show NMR results from two successive time points, separated by a “mixing” period, plotted against each other. The elements along the diagonal represent those that do not undergo exchange, while off-diagonal points represent spins that exchange due to magnetization transfer.

From these measurements, three major components were determined. The off-resonance component that did not wash out with D_2O immersion and had a relatively slow relaxation rate was determined to be from lipids. The extremely short relaxation rate component was determined to be from a combination of collagen and mineral sources. The component of the spectrum from T_2 s in the millisecond-second range was derived mostly from pore water and water bound to the bone matrix collagen.

On clinical MRI scanners, T_2 can not be measured because the echo time needed for a spin echo sequence is typically too long to measure these short T_2 components, so T_2^* values were used instead. Population average T_1 values were found by measuring T_1 - T_2 spectra using IR-CPMG, and population average T_2^* values were found using biexponential fitting of the free induction decay (FID) signal magnitude. Bound water was found to have a T_2^* on the order of 400 μs at 4.7T and pore water was found to have a broad spectrum of T_2^* values averaging 1280 μs at 4.7T (26).

1.2.2 NMR of Cortical Bone and Mechanical Properties

These NMR measurements of collagen, bound water, and pore water led to the determination of correlations of these measurements with mechanical properties (27). Cortical bone samples were taken from 40 human femurs, and divided into three segments. One segment was used for NMR measurements using the same CPMG ^1H NMR measurements described in 1.2.1 to determine proton concentrations from bound water, pore water, and collagen. Another bone segment was used for micro-CT (μCT) measurements to compare NMR measures to X-ray measures for fracture risk prediction. The third segment was used for mechanical testing to measure four properties: yield stress, peak stress, flexural modulus, and pre-yield or elastic toughness. The NMR signals from collagen, bound water, and pore water showed a strong linear correlation with mechanical properties of bone, though the net signal did not. The NMR measures were found to be better predictors (higher correlation) than the μCT measures in three of the four measured mechanical properties. In particular, bones with a greater concentration of bound water and a lower concentration of pore water were found to have generally greater mechanical properties (i.e., higher values of peak stress, yield stress and pre-yield toughness). However, because the bound water and pore water concentration had opposite relationships to mechanical properties, NMR measures that included signal from both bound and pore water had relatively weak predictive values of mechanical properties.

These results suggest that appropriate MRI methods that robustly distinguish and quantitatively measure bound- and pore-water concentrations in cortical bone may offer a viable methodology for predicting fracture risk. In particular, they can assess the contribution of the bone tissue to fracture resistance in addition to the structural

contribution already provided by conventional MRI or X-ray computed tomography. This is potentially quite useful since clinical assessment of areal bone mineral density by dual-energy X-ray absorptiometry does not necessarily capture all the deleterious effects of aging and certain diseases (type 2 diabetes, chronic kidney disease) on fracture risk (2,28).

1.2.3 NMR of Cortical Bone and Adiabatic Pulses Methods

Bi-exponential analysis of T_2^* signal decays has shown correlations between the fitted components amplitudes and the bound and pore water concentrations (29–32). This approach requires noise-sensitive non-linear regression and may be limited at high static field strengths by the similarity of T_2^* of bound and pore water (23,26,33). An proposed alternative approach uses T_2 -selective adiabatic radiofrequency (RF) pulses over a broad enough resonance bandwidth to effectively distinguish bound- and pore-water signals (26). The pore water signal is distributed over a large bandwidth, and therefore needs to be inverted with a large bandwidth RF pulse. Conventional pulses have a constant carrier frequency that is applied at the center of the spectrum being excited.

Adiabatic pulses, or frequency modulated RF pulses, sweep through a range of carrier frequencies over the duration of the pulse. These pulses have the ability to encompass large bandwidths and long durations. Because they include a large range of frequencies, a large range of T_2 s can be selected using these adiabatic pulses. This is necessary when manipulating pore water signal because pore water contains a large range of T_2 s. However, adiabatic pulses do not have the conventional relationship between flip angle and B_1 amplitude. Instead, the direction of the magnetization stays the same as the direction of the effective B field, given that the adiabatic condition is maintained. The

adiabatic condition states that the effective magnetic field must change significantly more slowly than the rotation of the signal magnetization about the effective field. This means that the effective B_1 amplitude needs to be large relative to the rate of change of the angle of the effective B_1 over time. Consequently, the adiabatic condition in the presented pulses for selectively measuring bound and pore water is satisfied by using a high B_1 amplitude with a relatively long pulse duration.

With high B_1 and long pulse durations, the amount of power going into the tissue is relatively high. The specific absorption rate (SAR) is a measure of how much power is being absorbed by the tissue, and therefore how much heating the tissue experiences (usually limited to 1-3°C). Reducing SAR results in longer repetition times (TRs) and consequently longer scan times.

Two clinically compatible methods for distinguishing bound and pore water were developed (26). A hyperbolic secant (sech), adiabatic full passage (AFP) pulse rotates magnetization 180° over a range of frequencies. A preparatory AFP pulse will invert pore water while saturating the bound water. Playing two consecutive broad-bandwidth adiabatic full passage pulses will drive short T_2 magnetization (bound water) to saturation while rotating long T_2 magnetization (pore water) through 360°, leaving it essentially unaffected. This approach was previously called the Double Adiabatic Full Passage (DAFP) but here is referred to as Pore water Imaging by Relaxation selective Saturation (PIRS). To image bound water, a similar approach uses one adiabatic full passage pulse followed by an appropriate delay to invert and null pore water magnetization while the bound water magnetization experiences a saturation-recovery process. This approach was

previously called the Adiabatic Inversion Recover (AIR) but here is referred to as Bound water Imaging by Relaxation selective Nulling (BIRN).

PIRS and BIRN were tested on a set of cadaver bone samples using the non-imaging NMR measures discussed above with and without AFP preparation pulses. The AFP pulses used were 10 ms in duration and 3500 Hz bandwidth and were shown to measure signal that was largely composed of bound water (BIRN) or largely composed of pore water (PIRS). The development of these preparation pulse methods opened the door to practical imaging studies of whole bone.

I.3 MRI for Cortical Bone Imaging

I.3.1 Ultra-short Echo Time (UTE) Imaging

Conventional MRI is not well suited for imaging cortical bone signals because the T_2 is extremely short compared to the echo time (TE). Ultra-short echo time (UTE) imaging uses a spoiled gradient echo sequence and allows for acquisition of signals with T_2 times on the order of microseconds, and this has been successfully applied to cortical bone (29,30,34–38).

In this work, 3D UTE methods are used by applying short RF excitation pulses and acquiring radial trajectories from the center of k-space, or raw data space. The center of k-space contains the most information, so by acquiring from the center at each spoke, the majority of the data is collected quickly before the signal decays. This also helps to reduce motion artifacts, since there is a large amount of information near the center of k-space over the entire scan length. After the excitation, the read out gradient is ramped up rapidly to acquire the maximum amount of data. Typically, acquisition begins after the

gradient has finished ramping, but in this case, acquisition begins on the ramp (ramp sampling) to further shorten TE, so data acquisition can begin as soon as the excitation pulse is finished and the RF switching is completed. The radial trajectories are mapped prior to image acquisition, and after imaging, the data is density compensated using an iterative method and gridded on to Cartesian coordinates so that it can be reconstructed using standard discrete Fourier transform (DFT) methods (39).

The order of acquisition of the radial spokes, or views, is an important factor to consider. The view ordering used here was the same as presented by Wong (40), so that 3D k-space is traversed by acquiring radial spokes while spiraling up the z-axis. If acquired in one pass, each spoke is relatively close to the next, which could potentially lead to unwanted effects such as stimulated echoes and excitation from adjacent spokes. By acquiring the same number of radial spokes in multiple passes, this problem can be avoided because the spokes are more spread out in k-space.

1.3.2 Variable Flip Angle Approach

Acquiring multiple radial views with one preparation pulse significantly decreases scan time and accelerates acquisition, which is necessary when translating to practical human studies. Conventional Magnetization Prepared Rapid Gradient Echo (MP-RAGE) protocols (41) are commonly used for this purpose. If a constant flip angle is used over the course of the acquisitions, the transverse magnetization decreases with every acquisition. Radial trajectories are especially sensitive to these changes because the origin of k-space is sampled with every spoke. This leads to a variable flip angle approach, where the flip angle was varied over the acquisitions for one preparation pulse so that the transverse magnetization remains constant (42).

This can be analytically solved for by neglecting relaxation effects. Because the time between acquisitions is short (>3 ms), T_1 relaxation during the train of acquisitions is extremely small and can be neglected with minimal effects. For example, assuming bound water $T_1 = 350$ ms, the signal would decay by less than 1% per acquisition. This leads to a simple geometric relationship between the longitudinal magnetization (M_Z), the transverse magnetization (M_T), and the flip angle (θ):

$$M_Z(n + 1) = \sin \theta M_Z(n) \quad [1.1]$$

$$M_T(n + 1) = \cos \theta M_Z(n) \quad [1.2]$$

where n is the acquisition number. If flip angles over the course of the sequence are found such that the transverse magnetization is held constant over the train of acquisitions for a desired train length, an equation for θ can be solved for:

$$\theta(n) = \tan^{-1} (\sin(\theta(n + 1))) \quad [1.3]$$

This method maximizes the signal for greater SNR efficiency. This flip angle schedule and its effects on magnetization are demonstrated in Figure 1.

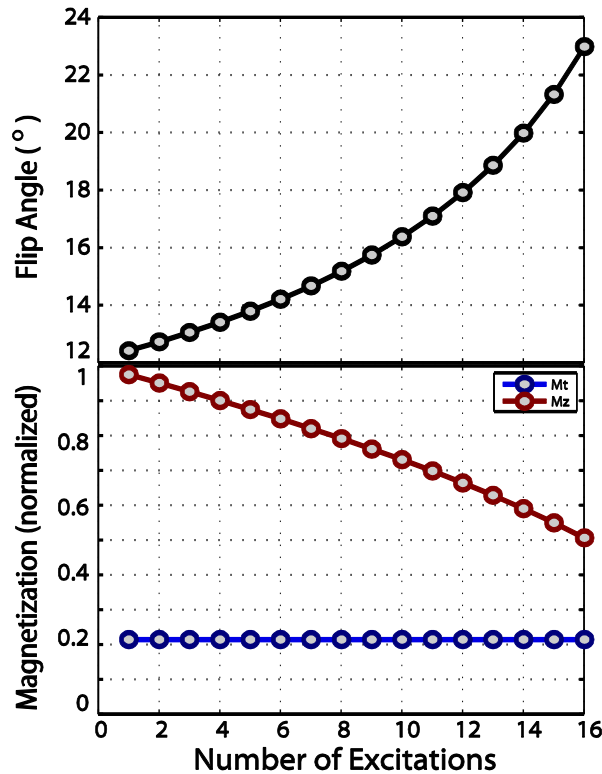


Figure 1: This diagram shows a sequence of 16 flips after one preparation pulse. The top graph shows the change in flip angle over the 16 acquisitions, ranging from 12.5° to 23° . The bottom graph shows the longitudinal (red) and transverse (blue) magnetization. This method holds the transverse magnetization constant over the course of the flip angles.

1.3.3 Signal Amplitude Correction for Blurring

Because the relaxation times of bound and pore water are similar to the acquisition duration, it is necessary to account for the effect of transverse relaxation during the acquisition on image signal amplitude. Relaxation during acquisition broadens the image-domain point spread function, which can blur a significant amount of signal out of the voxel or region of interest (ROI). With ramp sampling, this underestimation is exacerbated because the signal decays more rapidly in k-space. For the 3D bone imaging, the samples are roughly invariant in the direction of the long axis of the bone, so the blurring effect can be neglected in that direction. Also, because the k-space sampling is

radial, the point spread function can be solved in 1D, then applied in the 2D plane corresponding to the axial view of the bone (Fig 2).

This signal loss can be accounted for analytically from the point spread function for one voxel, or by simulating the effect this would have on a particular geometry. The amount of signal loss depends on the geometry of the sample being imaged; geometries with greater widths and more voxels have less signal loss than geometries with fewer voxels, so it is useful to compute this loss based on the geometry of the signal being measured.

For a known image geometry, $T_2^*(s)$, and k-space trajectory, the signal attenuation can be numerically estimated as follows: *i*) a masked 2D bone image, $s(\mathbf{r})$ (bone signal = 1, all other signal equals 0) is Fourier transformed to produce the k-space signal, $S(\mathbf{k})$; *ii*), the effect of T_2^* decay during acquisition is imparted by multiplying $S(\mathbf{k})$ by $H(\mathbf{k})$, derived below; *iii*) the resulting apodized signal is inverse Fourier transformed to produce a blurred image, $s_b(\mathbf{r})$; and *iv*) the signal loss term, β , is then computed on a voxel-by-voxel basis as $\beta = s_b(\mathbf{r})/s(\mathbf{r})$.

The apodizing function, $H(\mathbf{k})$, is derived for a 2D radial acquisition as follows. The signal decay during acquisition as a function of time is

$$h(t) = e^{-\frac{t}{T_2^*}}, \quad [1.4]$$

and k is a function of t by the relationship:

$$|k(t)| = \frac{\gamma}{2\pi} \int_0^t g(t') dt', \quad [1.5]$$

where γ is the gyromagnetic ratio and $g(t)$ is the gradient waveform. In this case, ramp sampling needs to be included in this calculation. Assume that $g(t)$ increases linearly at a constant slew rate up to max gradient amplitude G , at time $t = t_0$, then,

$$|k(t)| = \begin{cases} \frac{\gamma}{2\pi} \frac{Gt^2}{2t_0} & t < t_0 \\ \frac{\gamma}{2\pi} G \left(t - \frac{t_0}{2} \right) & t \geq t_0 \end{cases} \quad [1.6]$$

Let $k_0 = k(t_0) = \frac{\gamma}{4\pi} G t_0$, then

$$t = \begin{cases} \sqrt{\frac{4\pi t_0 |k|}{\gamma G}} & k < k_0 \\ \frac{2\pi |k|}{\gamma G} + \frac{t_0}{2} & k \geq k_0 \end{cases}, \quad [1.7]$$

Substituting [1.7] into [1.4] gives the apodizing function in k-space

$$H(\mathbf{k}) = \begin{cases} e^{\sqrt{\frac{4\pi |k|}{\gamma G}}/T_2^*} & |k| < k_0 \\ e^{\left[\frac{2\pi |k|}{\gamma G} + \frac{t_0}{2} \right]/T_2^*} & |k| \geq k_0 \end{cases} \quad [1.8]$$

Now this point spread function can be applied to the k-space signal to estimate the signal decay in a known geometry. This is illustrated in Figure 2, where a masked bone slice (bone signal = 1, all other signal equals 0) is Fourier transformed, the resulting k-space is apodized by multiplying by $H(k)$ and then inverse Fourier transformed back to image space. The amount of signal loss, β can be estimated by evaluating the percent decrease in signal in a particular ROI.

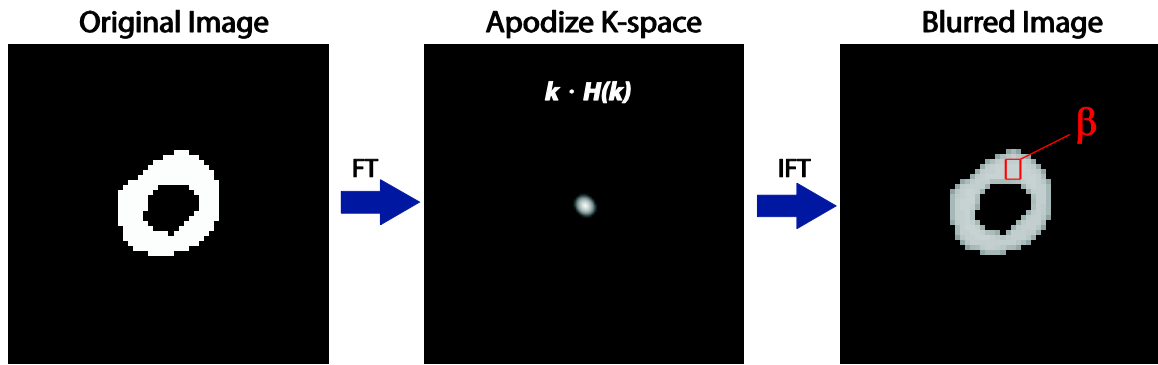


Figure 2: Estimated signal loss due to relaxation induced blurring. The masked 2D image of 1s and 0s is Fourier transformed to k-space, where the signal is multiplied by the apodizing function and then inverse Fourier transformed back to image space. The resulting image shows the amount of signal lost, and β is calculated based on the region of interest.

1.3.4 Bound and Pore Water Imaging

Combining the 3D UTE methods with the preparatory BIRN and PIRS pulse gives quantitative bound and pore water images. These imaging methods were demonstrated and validated on human cadaver bones, using clinically practical parameters, on both a 4.7T small-bore and a 3.0T human system.

CHAPTER II

MATERIALS AND METHODS

The Vanderbilt Donor Program supplied human femurs from 3 cadaveric donors, two males and one female, mean age 77 years. Mid-shaft sections of each bone were cut to \approx 80 mm in length. Images of the femur mid-shafts along with a CuSO_4 -doped water phantom (in a 10 mm NMR tube adjacent to the bone) were acquired using the PIRS and BIRN sequences, detailed below, with $96 \times 96 \times 96 \text{ mm}^3$ field of view and a nominal isotropic resolution of 1.5 mm. Imaging was performed on both a 3 T Philips Ingenia (Best, NL) and a 4.7 T Agilent Direct Drive (Santa Clara, CA). After imaging, cylindrical cortical bone samples (4-9 mm length, 6 mm diameter) were cored from four radial locations near the middle of the mid-shaft. These samples, along with a long- T_2 water sample of known volume, were used to provide reference values of bound and pore water concentrations using a previously described CPMG protocol (26) at 4.7 T.

II.1 Pulse Sequences

Figure 3 shows sequence diagrams of the PIRS and BIRN sequences. In all cases, the following sequence parameters were used: radial acquisitions of 83 points at 250 kHz receiver bandwidth, acquisition time per spoke = 332 μs ; a post-acquisition spoiler gradient 1.74 ms duration and 31 mT/m amplitude; repetition time per spoke (TR_A) = 3.18 ms; number of spokes per TR (N_S) = 16; total number of spokes = 8192; RF

excitation pulse width = 115 μ s. A variable flip angle schedule was used for excitations in order to generate approximately constant transverse magnetization for all 16 spokes (42), with an initial prescribed flip angle, $\theta_1 = 12.5^\circ$, and effective total flip angle, $\theta_E = 60^\circ$ (i.e., longitudinal magnetization is reduced by $\cos(\theta_E)$ by the combination of all 16 excitations). In all cases, the effective echo time (TE), as measured from the center of the RF pulse to the start of acquisition was 105.5 μ s (4.7T) and 127.5 μ s (3.0T).

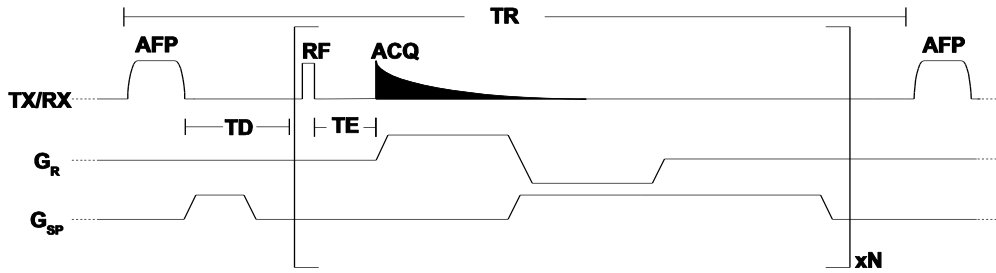


Figure 3: The 3D-UTE pulse sequence used. The PREP pulse is a double HS8 pulse for PIRS and a single HS8 pulse for BIRN. TD is the time delay between the application of the preparation pulse and the start of data acquisition. The effective inversion-recovery time $TI = TD + TR_A * N/2$, where N = number of pulses in the echo train length and TR_A = repetition time between multiple excitations.

The BIRN sequence used $TR = 300$ ms, $TI = 90\text{ms}/85\text{ms}$ (4.7T/3T), and a 10-ms duration, 3.5 kHz bandwidth, 8th ordered hyperbolic secant (HS8) pulse (43) as the preparation pulse. The PIRS sequence used $TR = 400$ ms, $TD = 5$ ms, and two consecutive HS8 pulses (20 ms total duration). The maximum gradient amplitudes and slew rates of the human system were also used on the 4.7T. Likewise, the TR values for each sequence were dictated by FDA-defined RF power deposition limits on the 3.0T scanner. On the 4.7T system, one excitation provided sufficient signal, resulting in scan times of $\approx 3 \frac{1}{2}$ min and $\approx 2 \frac{1}{2}$ min for PIRS and BIRN, respectively. On the 3.0T system,

lower signal-to-noise ratio (SNR) dictated 4 averaged excitations ($\approx 13 \frac{1}{2}$ m) for PIRS and 6 averaged excitations ($\approx 20 \frac{1}{2}$ m) for BIRN.

In addition, a conventional UTE (CUTE) image was acquired for each bone at 3.0T and 4.7T, and at 4.7T a B1 map was also acquired. The CUTE acquisition used TR/TE = 2.5 ms/62.5 μ s and a 25 μ s duration, 6° flip excitation pulse. The B₁ mapping was performed by the Bloch-Siegert method (44) with a multi-slice spin echo acquisition. Ten axial slices (3 mm thick/5 mm gap) spanned the length of the bone. The B₁ measured in the water phantom of each slice was used to determine the actual flip angle seen in each slice for analysis of BIRN and PIRS data (see below). Variation of |B₁| within the slice was independently determined to be < 2.5% for the coil used on the 4.7T. On the 3.0T, the body RF coil was used for transmission and was independently determined to vary in |B₁| by <4.5% over the entire bone volume, so no B1 mapping was necessary.

II.2 Data Analysis

All data were analyzed using MATLAB (Natick, MA). Images were reconstructed using standard trajectory mapping, density compensation, and gridding methods (39). Bound and pore water concentrations were computed on a voxel-by-voxel basis, as described below, then ROIs were defined at the approximate locations from which the cylindrical bone samples were taken. The signal equations for PIRS and BIRN measurements in cortical bone are shown below (note the correction in Eq [2.1], compared with a previous report (26)):

$$S_{\text{PIRS}} \approx S_0^{\text{PW}} \beta^{\text{PW}} \sin \theta_1 \frac{(\alpha^{\text{PW}})^2 (1 - e^{-R_1^{\text{PW}} \text{TR}})}{1 - (\alpha^{\text{PW}})^2 e^{-R_1^{\text{PW}} \text{TR}} \cos \theta_E} e^{-R_2^{*\text{PW}} \text{TE}}, \quad [2.1]$$

and

$$S_{\text{BIRN}} \approx S_0^{\text{bw}} \beta^{\text{bw}} \sin \theta_1 \frac{1 - (1 - \alpha^{\text{bw}}) e^{-R_1^{\text{bw}} T_I} - \alpha^{\text{bw}} e^{-R_1^{\text{bw}} T_{\text{TR}}}}{1 - \alpha^{\text{bw}} e^{-R_1^{\text{bw}} T_{\text{TR}} \cos \theta_E}} e^{-R_2^* \text{bw} T_E}, \quad [2.2]$$

where α is the inversion efficiency of the AFP pulse, β is the signal loss due to relaxation-induced blurring, S_0 is proportional to water concentration, and superscripts ^{pw} and ^{bw} indicated pore water and bound water, respectively. Replacing ^{pw} or ^{bw} with ^{ref}, provides the signal equations for the reference marker for each sequence.

At 4.7 T, previously obtained values were used for inversion efficiency (α), R_1 , and R_2^* of bound water, pore water, and the reference marker (26): $\alpha^{\text{bw/pw/ref}} = 0.09/-0.78/-0.83$, $1/R_1^{\text{bw/pw/ref}} = 357 \text{ ms}/551 \text{ ms}/13 \text{ ms}$, $1/R_2^{*\text{bw/pw/ref}} = 290 \text{ }\mu\text{s}/1280 \text{ }\mu\text{s}/13 \text{ ms}$. At 3.0 T, R_1^{pw} was estimated from one bone using a saturation-recovery fast spin echo acquisition, and R_1^{bw} was estimated to change similarly from 4.7T as did R_1^{pw} . The R_2^* values at 3.0 T were used as measured by Du et al. for ex vivo human cortical bone (31). Because R_2 values were assumed to be nearly B_0 independent, the same α values were used at 3T as were previously measured at 4.7 T. A summary of parameter values used at 3T are $\alpha^{\text{bw/pw/ref}} = 0.09/-0.78/-0.83$, $1/R_1^{\text{bw/pw/ref}} = 290 \text{ ms}/450 \text{ ms}/10 \text{ ms}$, $1/R_2^{*\text{bw/pw/ref}} = 350 \text{ }\mu\text{s}/2600 \text{ }\mu\text{s}/10 \text{ ms}$.

The blurring-induced signal loss values (β) were empirically estimated by simulating the effect of blurring using the known bone geometry for each bone, as explained in section 1.2.3. Individual β values were found for each ROI and each bone, but mean estimates used to create images were $\beta^{\text{bw/pw}} = 0.77/0.97$ at 3.0 T and $0.74/0.93$ at 4.7 T. In both cases, β^{ref} was defined = 1.0.

Thus, given the observed bone signals S_{PIRS} and S_{BIRN} , the equilibrium signals, S_0^{pw} and S_0^{bw} were computed from each bone using Eq [2.1] and [2.2]. The relative measures

of proton density were then converted into absolute units of mol $^1\text{H}/\text{L}_{\text{bone}}$ by comparison to corresponding values of S_0^{ref} , which were known to reflect 111.1 mol $^1\text{H}/\text{L}_{\text{H}_2\text{O}}$. This was simply done by taking the result of $111.1 * S_0^{\text{pw/bw}}/S_0^{\text{ref}}$.

The non-imaging data from the extracted cortical bone samples were analyzed by fitting CPMG echo amplitudes to a broad range of decaying exponential functions by non-negative least squares criteria subject to a minimum curvature constraint, resulting in a T_2 -spectrum for each sample (23,45). The integrated T_2 spectrum amplitude over various domains provided signal amplitude measures for bound water ($100 \mu\text{s} < T_2 < 1 \text{ms}$), pore water ($1 \text{ms} < T_2 < 1 \text{s}$) and reference sample ($T_2 > 1 \text{s}$). The bound and pore water signal amplitudes were then converted into units of mol $^1\text{H}/\text{L}_{\text{bone}}$ by comparison with the reference signal amplitude and known volumes of the bone and reference samples, and the known proton concentration of water, as above.

CHAPTER III

RESULTS

Figure 4 shows approximately the same slice taken from 3D bound and pore water images of one bone at both 3T and 4.7T. The gray scale images are conventional UTE images; color overlaid images are the bound or pore water concentration map generated from the respective method.

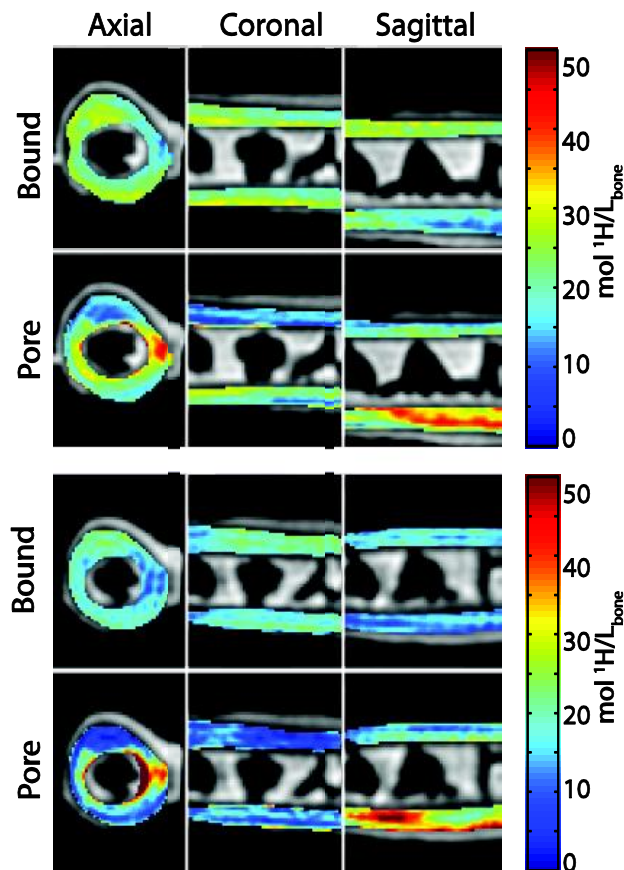


Figure 4: Imaging results from 3T (top) and 4.7T (bottom) of the PIRS and BIRN sequences showing three planes of pore and bound water maps. Note the negative correlation between bound and pore water throughout the bone volume and the higher concentration of pore water in the posterior section of the femur (lower sagittal image).

The PIRS image shows consistently a higher concentration of pore water in the posterior section of the femur, which agrees with previous findings (46,47), and in general there is an apparent negative correlation between the spatial distribution of bound and pore water, as expected. The signal to noise ratios (SNR) of PIRS/BIRN images were $\sim 27/\sim 22$ at 4.7T and $\sim 26/\sim 28$ at 3.0T, measured assuming a Rayleigh distribution with $SNR = \mu_S/(\mu_N/\sqrt{\pi/2})$, where μ_S is the mean signal from an area of cortical bone, and μ_N is the mean signal from a small area of noise. (At 3.0T, the background of the BIRN images showed significant signal from the foam used to hold the bone samples, so for this SNR measure one scan was repeated with a larger FOV but equal voxel size and receiver bandwidth).

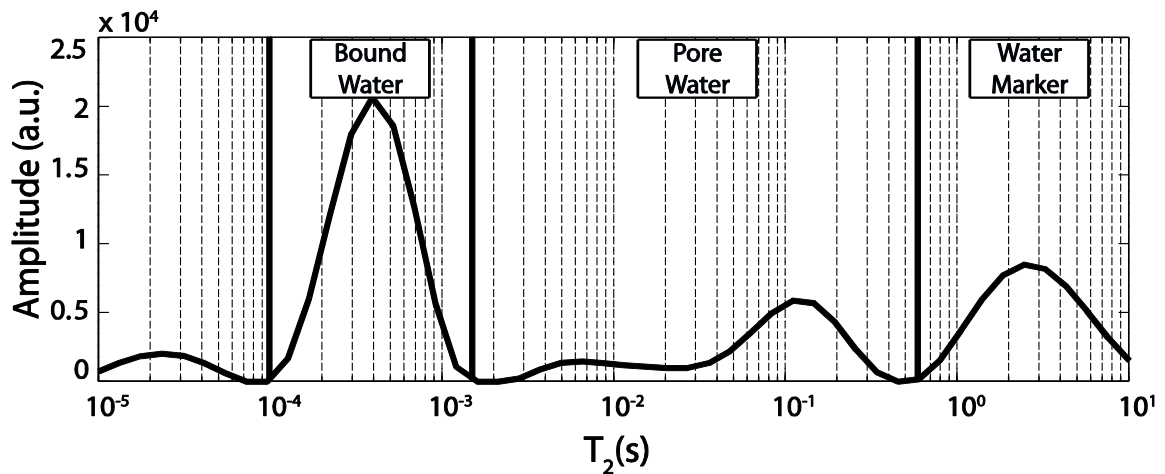


Figure 5: A representative T_2 spectrum from the CPMG measurements of the cored samples of cortical bone showing signals from bound water, pore water, and the water marker. The amount of bound and pore water was converted into units of mol $^1\text{H/L}$ based on the known size and concentration of the water marker.

Figure 5 shows a representative T_2 spectrum from an extracted cortical bone sample, with the bound water, pore water, and water marker signals labeled. Figure 6 shows generally strong linear correlations between bound/pore water concentration measures from the extracted samples and those from the BIRN and PIRS images at approximate locations of the extracted bone samples (shown by red squares on inset image). Coefficients of determination for pore water concentrations were $r^2 = 0.41$ at 3T and $r^2 = 0.94$ at 4.7T; for bound water concentrations they were $r^2 = 0.79$ at 3T and $r^2 = 0.57$ at 4.7T.

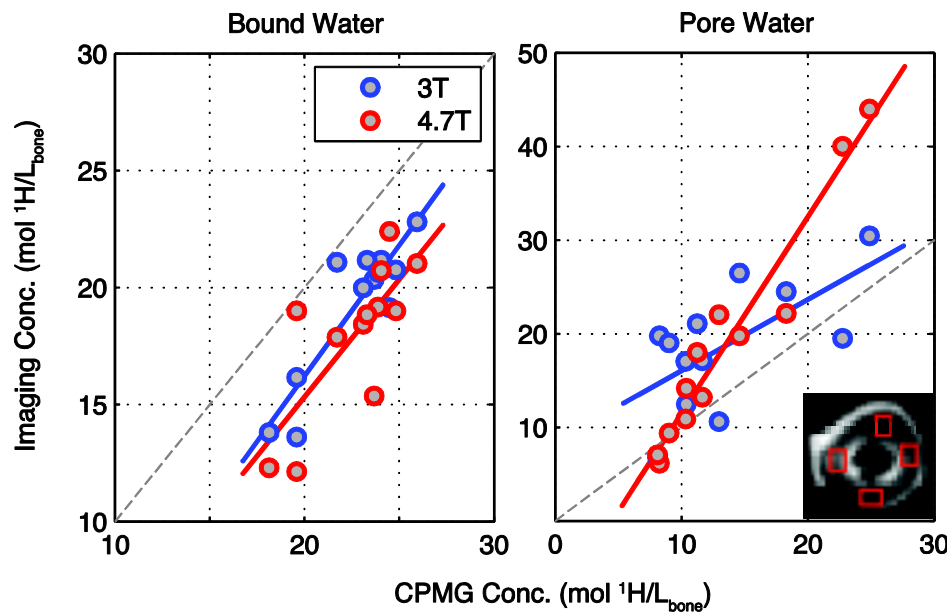


Figure 6: Concentrations from CPMG measurements versus PIRS and BIRN results at approximate sample locations from 3T and 4.7T images of a) bound water and b) pore water. Both 3T and 4.7T imaging measurements showed strong linear correlations with CPMG measurements.

CHAPTER IV

DISCUSSION AND CONCLUSIONS

The magnetization preparations used in the BIRN and PIRS pulse sequences were previously demonstrated to effectively distinguish bound and pore water signals in isolated human cortical bone samples (26). Presented here is the translation of these methods into clinically practical MRI protocols, and the quantitative evaluation of these MRI protocols on human cadaver bones at 3.0 and 4.7 T. The results suggest that the BIRN and PIRS methods are effective for quantitative imaging of bound and pore water, respectively, but there are numerous factors that may affect their performance and utility.

First, in contrast to previous non-localized studies of isolated bone samples, the imaging protocols presented here required accelerated acquisition to maintain scan times that are amenable for human studies. Both BIRN and PIRS scans utilized 16 radial acquisitions of k-space per TR period, similar to a conventional MP-RAGE protocol (48). Acquiring more than 16 spokes per magnetization preparation is possible in principle, but will require a lower excitation flip angle and introduce increasing amounts of longitudinal recovery of the nulled/saturated magnetization. Unlike scans using a Cartesian k-space trajectory, where the origin of k-space is sampled only once per image, the 3D radial trajectories here sampled the k-space origin with every radial spoke. Consequently, accurate quantitation of image signal intensity was aided by using a variable excitation flip angle schedule (42) across the 16 spokes per TR such that each spoke measured approximately the same amplitude of transverse magnetization at the k-space origin. The resulting scan times at 3.0T of ≈ 13 and ≈ 20 minutes for the BIRN and PIRS sequences

were limited by RF power deposition from AFP pulses. Previous work suggests that it might be possible to reduce the AFP pulse bandwidth (and hence power deposition) by $\approx 2\times$ from the 3.5 kHz used here (26), which would allow further acceleration by reducing TR, although there will be a corresponding SNR penalty. Also, the use of parallel imaging and/or compressed sensing methods may further accelerate these acquisitions. Ultimately, the most effective approach to acceleration will be through 2D rather than 3D protocols. Slice selective UTE is possible through half pulse excitation (49–51), but signal amplitudes from these methods are very sensitive to gradient waveform calibration, making their use for quantitative methods a challenge.

In addition to scan time, practical use of the BIRN and PIRS protocols depends upon having good estimates of a number of parameters in the signal equations, Eq [2.1] and [2.2]. As done here for scans on the 4.7T, it is relatively quick and easy to map B_1 , thereby providing good estimates of θ_1 and θ_E on a case-by-case basis. However, estimates of bound- and pore-water relaxation rates cannot be obtained experimentally during a clinical protocol, so good population estimates are needed. The values used here and in a previous study (26) on a small sample of cadaver bones have been good enough to demonstrate efficacy of the BIRN and PIRS methods, but it is likely that errors in these values, or limitations of describing relaxation rates by single values, underlies the systematic deviations between imaging and CPMG measures seen in Figure 6. Given the parameters used in this work, an error of 10% in T_1 gives a 5/8% error of PIRS/BIRN signal, while a 10% error in T_2^* gives a 1/4% error of PIRS/BIRN signal. Further, it may not be suitable to describe R_1 and R_2^* with scalar values. In particular, pore water likely consists of a relatively broad spectrum of T_1 values due to the variation in pore sizes

within the bone (21,26), although the BIRN sequence need only null the net pore water magnetization not all the pore water, so this may not be a significant limitation.

Two parameters that are known but require special attention for accurate BIRN and PIRS measures are TE and receiver bandwidth. Although it is common to define TE from the end of the RF excitation pulse, the effect of relaxation during the RF pulse must be incorporated to ensure accurate measures. For hard pulse 3D UTE, as used here, transverse relaxation can be effectively accounted for by measuring TE from the middle of the RF pulse rather than the end (49). Accounting for transverse relaxation during the acquisition is a somewhat more complicated problem. Because the bound water T_2^* is similar to the acquisition duration (332 μs), its relatively broad point spread function results in an underestimation of bound water signal compared to signal from the long T_2 water reference. In the simple case of exponential decay along each radial spoke, bound water signal from an isolated voxel-sized piece of bone would be reduced by $\approx 0.74\times$. In practice, this signal loss is mitigated for larger regions of bone but exacerbated by ramp sampling. In the present studies, as noted in the MATERIALS AND METHODS, the bound and pore water signal losses were empirically estimated, which resulted in the $\beta^{\text{bw/pw}} = 0.77/0.97$ at 3.0 T and $0.74/0.93$ at 4.7 T.

These studies demonstrate the translation of previously developed approaches for distinguishing bound and pore water from human cortical bone. The methods, referred to as BIRN and PIRS here, were implemented as part of 3D UTE pulse sequences, subject to the practical human MRI constraints of gradient performance and RF power deposition. The results showed good correlation between these imaging measures of

bound and pore water and those determined by previously established non-localized CPMG measures.

REFERENCES

1. Burge R, Dawson-Hughes B, Solomon DH, Wong JB, King A, Tosteson A. Incidence and Economic Burden of Osteoporosis-Related Fractures in the United States, 2005–2025. *J Bone Miner Res.* 2007;22(3):465–75.
2. Kanis JA, Johnell O, Oden A, Dawson A, De Laet C, Jonsson B. Ten Year Probabilities of Osteoporotic Fractures According to BMD and Diagnostic Thresholds. *Osteoporosis Int.* 2001;12(12):989–95.
3. Van Der Klift M, De Laet C, McCloskey E, Hofman A, Pols H. The Incidence of Vertebral Fractures in Men and Women : The Rotterdam Study. *J Bone Miner Res.* 2002;17(6):1051–6.
4. Bonds DE, Larson JC, Schwartz A V, Strotmeyer ES, Robbins J, Rodriguez BL, et al. Risk of Fracture in Women with Type 2 Diabetes : the Women ' s Health Initiative Observational Study. *J Clin Endocr Metab.* 2006;91(9):3404–10.
5. Schwartz A V, Sellmeyer DE. Diabetes , Fracture , and Bone Fragility. *Current osteoporosis reports.* 2007;5(3):105–11.
6. Vestergaard P, Rejnmark L, Mosekilde L. Diabetes and Its Complications and Their Relationship with Risk of Fractures in Type 1 and 2 Diabetes. *Calcif Tissue Int.* 2009;84(1):45–55.
7. Wild S, Roglic G, Green A, Sicree R, King H. Global prevalence of diabetes: estimates for the year 2000 and projections for 2030. *Diabetes Care.* 2004;27(5):1047–53.
8. Manske SL, Liu-Ambrose T, Bakker PM, Liu D, Kontulainen S, Guy P, et al. Femoral neck cortical geometry measured with magnetic resonance imaging is associated with proximal femur strength. *Osteoporosis Int.* 2006;17(1):1539–45.
9. Black DM, Bouxsein ML, Marshall LM, Cummings SR, Lang TF, Cauley JA. Proximal Femoral Structure and the Prediction of Hip Fracture in Men: A Large Prospective Study Using QCT. *J Bone Miner Res.* 2008;23(8):1326–33.
10. Bouxsein ML. Technology Insight : noninvasive assessment of bone strength in osteoporosis. *Nat Clin Pract Rheum.* 2008;4(6):310–8.
11. Keyak JH, Rossi S a, Jones K a, Skinner HB. Prediction of femoral fracture load using automated finite element modeling. *J Biomech.* 1998 Feb;31(2):125–33.

12. Pistoia W, Van Rietbergen B, Lochmüller E-M, Lill C a, Eckstein F, Rügsegger P. Estimation of distal radius failure load with micro-finite element analysis models based on three-dimensional peripheral quantitative computed tomography images. *Bone*. 2002 Jun;30(6):842–8.
13. Crawford RP, Cann CE, Keaveny TM. Finite element models predict in vitro vertebral body compressive strength better than quantitative computed tomography. *Bone*. 2003 Oct;33(4):744–50.
14. Zioupos P, Currey JD, Hamer AJ. The role of collagen in the declining mechanical properties of aging human cortical bone. *J Biomed Mater Res*. 1999;45(2):108–16.
15. Wang X, Shen X, Li X, Agrawal CM. Age-related Changes in the Collagen Network and Toughness of Bone. *Bone*. 2002;31(1):1–7.
16. Graves CL, Smith DM. Membrane pore structure analysis via nmr spin-lattice relaxation experiments. *J Membrane Sci*. 1989;46:167–84.
17. Chui MM, Phillips RJ, McCarthy MJ. Measurement of the Porous Microstructure of Hydrogels by Nuclear Magnetic Resonance. *J Colloid Interf Sci*. 1995;174:336–44.
18. Kenyon WE. Petrophysical principles of applications of NMR logging. *Log Analyst*. 1997;38:21–43.
19. Wang X, Ni Q. Determination of cortical bone porosity and pore size distribution using a low field pulsed NMR approach. *J Orthopaed Res*. 2003 Mar;21(2):312–9.
20. Ni Q, Nicoletta DP. The characterization of human cortical bone microdamage by nuclear magnetic resonance. *Meas Sci Technol*. 2005 Mar 1;16(3):659–68.
21. Fantazzini P, Brown RJS, Borgia GC. Bone tissue and porous media: common features and differences studied by NMR relaxation. *Magn Reson Img*. 2003 Apr;21(3-4):227–34.
22. Ni Q, King JD, Wang X. The characterization of human compact bone structure changes by low-field nuclear magnetic resonance. *Meas Sci Technol*. 2004 Jan 1;15(1):58–66.
23. Horch RA, Nyman JS, Gochberg DF, Dortch RD, Does MD. Characterization of ¹H NMR signal in human cortical bone for magnetic resonance imaging. *Magn Reson Med*. 2010 Sep;64(3):680–7.
24. Meiboom S, Gill D. Modified SpinEcho Method for Measuring Nuclear Relaxation Times. *Rev. Sci. Instrum*. 1958;29(8):688–91.

25. Callaghan PT, Arns CH, Galvosas P, Hunter MW, Qiao Y, Washburn KE. Recent Fourier and Laplace perspectives for multidimensional NMR in porous media. *Magn Reson Img.* 2007;25:441–4.
26. Horch RA, Gochberg DF, Nyman JS, Does MD. Clinically compatible MRI strategies for discriminating bound and pore water in cortical bone. *Magn Reson Med.* 2012; 68(6):1774–84.
27. Horch RA, Gochberg DF, Nyman JS, Does MD. Non-invasive predictors of human cortical bone mechanical properties: T(2)-discriminated H NMR compared with high resolution X-ray. *PloS one.* 2011 Jan;6(1):e16359.
28. Vestergaard P. Discrepancies in bone mineral density and fracture risk in patients with type 1 and type 2 diabetes--a meta-analysis. *Osteopros Int.* 2007 Apr;18(4):427–44.
29. Bae WC, Chen PC, Chung CB, Masuda K, D’Lima D, Du J. Quantitative ultrashort echo time (UTE) MRI of human cortical bone: correlation with porosity and biomechanical properties. *J Bone Miner Res.* 2012 Apr;27(4):848–57.
30. Diaz E, Chung CB, Bae WC, Statum S, Znamirovski R, Bydder GM, et al. Ultrashort echo time spectroscopic imaging (UTESI): an efficient method for quantifying bound and free water. *NMR Biomed.* 2012 Jan;25(1):161–8.
31. Du J, Hermida JC, Diaz E, Corbeil J, Znamirovski R, D’Lima DD, et al. Assessment of cortical bone with clinical and ultrashort echo time sequences. *Magn Reson Med.* 2012 Sep; in press available online, doi: 10.1002/mrm.24497.
32. Du J, Diaz E, Carl M, Bae W, Chung CB, Bydder GM. Ultrashort echo time imaging with bicomponent analysis. *Magn Reson Med.* 2012 Mar;67(3):645–9.
33. Ong HH, Wright AC, Wehrli FW. Deuterium nuclear magnetic resonance unambiguously quantifies pore and collagen-bound water in cortical bone. *J Bone Miner Res.* 2012 Jul 13;27(12):2573–81.
34. Robson MD, Gatehouse PD, Bydder M, Bydder GM. Magnetic Resonance: An Introduction to Ultrashort TE (UTE) Imaging. *J Comput Assist Tomo.* 2003;27(6).
35. Techawiboonwong A, Song HK, Leonard MB, Wehrli FW. Cortical Bone Water: in vivo quantification with ultrashort echo-time MR imaging. *Radiology.* 2008;248(3).
36. Techawiboonwong A, Song HK, Wehrli FW. In vivo MRI of submillisecond T 2 species with two-dimensional and three-dimensional radial sequences and applications to the measurement of cortical bone water. *NMR Biomed.* 2008;21:59–70.

37. Du J, Carl M, Bydder M, Takahashi A, Chung CB, Bydder GM. Qualitative and quantitative ultrashort echo time (UTE) imaging of cortical bone. *J Magn Reson.* Elsevier Inc.; 2010 Dec;207(2):304–11.
38. Rad HS, Lam SCB, Magland JF, Ong H, Li C, Song HK, et al. Quantifying cortical bone water in vivo by three-dimensional ultra-short echo-time MRI. *NMR Biomed.* 2011 Aug;24(7):855–64.
39. Zwart NR, Johnson KO, Pipe JG. Efficient sample density estimation by combining gridding and an optimized kernel. *Magn Reson Med.* 2012 Mar;67(3):701–10.
40. Wong STS, Roos MS. A strategy for sampling on a sphere applied to 3D selective RF pulse design. *Magn Reson Med.* 1994 Dec;32(6):778–84.
41. Mugler JP, Brookeman JR. Three-dimensional magnetization-prepared rapid gradient-echo imaging (3D MP RAGE). *Magn Reson Med.* 1990 Jul;15(1):152–7.
42. Haacke EM, Brown RW, Thompson MR, Venkatesan R. *Magnetic Resonance Imaging - Physical Principles and Sequence Design.* 1999. p. 463–5.
43. Garwood M. Improved Performance of Frequency-Swept Pulses Using Offset-Independent Adiabaticity. *J Magn Reson.* 1996;120:133–7.
44. Sacolick LI, Wiesinger F, Hancu I, Vogel MW. B1 mapping by Bloch-Siegert shift. *Magn Reson Med.* 2010 May;63(5):1315–22.
45. Whittall KP, MacKay AL. Quantitative interpretation of NMR relaxation data. *J Magn Reson.* 1989 Aug;84(1):134–52.
46. Fernández-Seara M a, Wehrli SL, Takahashi M, Wehrli FW. Water content measured by proton-deuteron exchange NMR predicts bone mineral density and mechanical properties. *J Bone Miner Res.* 2004 Feb;19(2):289–96.
47. Currey JD, Brear K, Zioupos P. The Effects of Ageing and Changes in Mineral Content in Degrading the Toughness of Human Femora. *J Biomech.* 1996;29(2):257–60.
48. Mugler JPI, Epstein FH, Brookeman JR. Shaping the Signal Response during the Approach to Steady State in Three-Dimensional Magnetization-Prepared Rapid Gradient-Echo Imaging Using Variable Flip Angles. *Magn Reson Med.* 1992;28:165–85.
49. Robson MD, Gatehouse PD. Consequences of T2 relaxation during half-pulse slice selection for ultrashort TE imaging. *Magn Reson Med.* 2010 Aug;64(2):610–5.

50. Larson PEZ, Gurney PT, Nayak K, Gold GE, Pauly JM, Nishimura DG. Designing long-T2 suppression pulses for ultrashort echo time imaging. *Magn Reson Med.* 2006 Jul;56(1):94–103.
51. Du J, Bydder M, Takahashi AM, Chung CB. Two-dimensional ultrashort echo time imaging using a spiral trajectory. *Magn Reson Img.* 2008 Apr;26(3):304–12.